

# On the stability and sound of an unforced flag

A. Manela<sup>a,\*</sup>, M.S. Howe<sup>b</sup>

<sup>a</sup>*Department of Mathematics, Massachusetts Institute of Technology, Cambridge, MA 02139, USA*

<sup>b</sup>*College of Engineering, Boston University, 110 Cummington Street, Boston MA 02215, USA*

Received 21 April 2008; received in revised form 1 October 2008; accepted 1 October 2008

Handling Editor: P. Joseph

Available online 28 November 2008

---

## Abstract

A linear theory is proposed for the motion and sound production of a flag in nominally uniform high Reynolds number flow. The flag is modelled as an elastic fluid-loaded filament subject to either clamped-free or fixed-free boundary conditions. Eigenfunctions describing standing waves in the absence of fluid loading are used to expand the loaded flag deflection. The resulting temporal stability problem is analysed and the neutral curve and modes of motion describing the transition to instability are discussed in detail for each boundary condition. It is found that the fixed-free flag is considerably more stable than the clamped-free flag. In the limit of a very heavy flag, instability sets in as a resonant standing wave, while lighter flags exhibit flutter (convective) instability. Acoustic radiation of dipole type is calculated and discussed in the limit where the flag is acoustically compact. At the onset of instability it is found that the acoustic pressure is dominated by the contribution from the wake and that light flags are noisier than heavy.

© 2008 Elsevier Ltd. All rights reserved.

---

## 1. Introduction

The fundamental fluid–structure interactions involved in the motion of a flag are of continuing and intense interest [1]. It is probably the simplest of a whole range of related mechanical problems that include, for example, the fluttering associated with both snoring [2] and the instabilities encountered in industrial printing machines [3]. Similar flapping motions are known to improve the efficiency of propulsive swimming [4], and are believed to reduce turbulent drag during locomotion [5].

Taneda [6] has investigated the motion of a flag experimentally in a wind tunnel. Zhang et al. [7] and Zhu and Peskin [8] have examined an analogue problem involving flexible filaments in flowing soap films. Watanabe et al. [3,9] examined the fluttering motion of paper both experimentally and numerically, using a time-marching scheme applied to the full Navier–Stokes equations and a low-order eigenfunction expansion assuming the flow is potential. More recently Shelley et al. [10] experimented with a flag in a water tunnel and compared their observations with predictions of ‘heavy-flag’ theory. A linearised treatment for the problem has been suggested by Argentina and Mahadevan [11], where a simplified mathematical description of the fluid loading effect was assumed based on classical thin airfoil theory [12]. Connell and Yue [13] have devised a

---

\*Corresponding author. Tel.: +1 617 324 2597; fax: +1 617 253 8911.

E-mail address: [avshalom@math.mit.edu](mailto:avshalom@math.mit.edu) (A. Manela).

nonlinear, numerical scheme that couples the flag motion to an incompressible wind governed by the Navier–Stokes equations. Alben and Shelley [14] have also considered the nonlinear dynamics of the flag, predicting phenomena such as bistability and transition to chaos. Fitt and Pope [15] have studied the case of a “stiff” flag in air incident at a finite angle of attack.

Most of these studies model the flag as a thin elastic membrane. The flag equation of motion then involves a balance between flag inertia, fluid loading, and a fourth order derivative of the flag displacement representing the stiffness response. The validity of such a formulation for a cloth flag is questionable, because a non-dimensional representation of the stiffness contribution reveals it to be small over its whole length (except possibly in the immediate neighbourhood of the free end). Yet, as some of the above studies indicate (see, e.g., [13]), it appears to be necessary to retain stiffness in the equation of motion to ensure robustness of the structural numerical model. Physically, it is not the introduction of this term into the equation that matters but the consequent requirement to impose four boundary conditions.

The effect of the end conditions on the resulting motion is crucial. Most of the aforementioned studies consider a “clamped-free” flag, where a vanishing deflection and angle of deflection are assumed at the pole. However, casual observation indicates that the latter may not be appropriate in practice. Fitt and Pope [15] have studied the effect of replacing the clamped condition with a fixed end condition where the bending moment should vanish at the pole. In this paper we also examine the effect of replacing the clamped-free condition by the more appropriate “fixed-free” condition, with the objective of calculating its influence on the sound produced by the motion of the flag. Special care must be given to vortex shedding from the flag trailing edge and the satisfaction of the Kutta condition, which turns out to be of dominant importance in the resulting acoustic field. This may be contrasted with the approach of Fitt and Pope [15] who assumed the wake to have only a small impact on the flag motion.

We consider the linearised problem and make use of the simplified fluid loading model suggested by Theodorsen [12] and applied by Argentina and Mahadevan [11]. The mathematical problem is formulated in Section 2. The corresponding eigenvalue problem for the self-excited motion and its outcome, the critical conditions for transition to flapping motion, are discussed in Section 3. In Section 4 the acoustic radiation is calculated for a compact flag. Some concluding remarks are made in Section 5.

## 2. The governing equations

Consider nominally uniform flow of air of mean density  $\rho_0$  at speed  $U$  over an inextensible flag of streamwise length  $L$  and mass  $\rho_s$  per unit area (Fig. 1). In the undisturbed state the flag occupies the interval  $0 < x^* < L$  of the  $x^*$  axis, has thickness  $h$  and span  $l$ , where  $h \ll l \ll L$ , and is connected to a flag pole at  $x^* = 0$ , where  $x^*$  is measured in the direction of the mean flow. The motion is assumed to be two-dimensional, uniform with respect to spanwise position parallel to the flag pole, and of high Reynolds number  $UL/\nu \gg 1$ , where  $\nu$  is the kinematic viscosity of the air. For simplicity, we neglect the effect of frictional drag. Small amplitude deflections  $\zeta^*(x^*, t^*)$  of the flag from an undisturbed planar form (in the direction of the  $y^*$ -axis normal to the undisturbed plane of the flag) are taken to be governed in the linearised approximation by

$$\rho_s \frac{\partial^2 \zeta^*}{\partial t^{*2}} + EI \frac{\partial^4 \zeta^*}{\partial x^{*4}} - \Delta p^* = 0, \tag{1}$$

where  $EI$  is the bending stiffness of the flag ( $E$  being Young’s modulus and  $I = h^3/12$  the moment of inertia coefficient per unit span) and  $\Delta p^* = p_-^* - p_+^*$  is the inertial pressure loading (representing the ‘added mass’ as well as vortex shedding effects) in the direction of positive  $\zeta^*$  (Fig. 1). A dimensionless representation of the



Fig. 1. Setup of the problem. The flag pole is located at  $x^* = 0$  and its free end is at  $x^* = L$ . The inertial fluid loading is  $\Delta p^* = p_-^* - p_+^*$  and the circulation per unit length of the shedded vortex sheet is  $\gamma^*(x^*, t^*)$ .

problem is achieved by normalizing distances by the flag length  $L$  and pressure by  $\rho_0 U^2$ . To obtain a dimensionless balance between inertial and elastic effects we scale the time by  $L/U_b$ , where  $U_b = \sqrt{EI/\rho_s L^2}$  is the characteristic bending wave velocity. Substituting these into Eq. (1) and denoting non-dimensional variables by the omission of asterisks, we have

$$\frac{\partial^2 \xi}{\partial t^2} + \frac{\partial^4 \xi}{\partial x^4} - \frac{\alpha^2}{\mu} \Delta p = 0, \tag{2}$$

where  $\mu = \rho_s/\rho_0 L$  is the non-dimensional flag mass and  $\alpha = U/U_b$  the normalised wind speed.

*2.1. Calculation of  $\Delta p$*

The inertial pressure jump  $\Delta p$  is predominantly attributable to the effect of added mass, and is determined as a superposition of non-circulatory (nc) and circulatory (c) flows associated, respectively, with the potential flow motion of the relatively large scale flow induced by the motion of the flag and vortex shedding from the flag trailing edge. Assuming a slowly varying transverse velocity of the fluid along the filament, we make use of the approximate airfoil theory of Theodorsen [12] and write for the non-circulatory velocity potential (scaled by  $LU$ ) along the flag

$$\phi_{nc} = \pm \sqrt{x(1-x)} \left( \frac{1}{\alpha} \frac{\partial \xi}{\partial t} + \frac{\partial \xi}{\partial x} \right). \tag{3}$$

The positive and negative signs correspond, respectively, to the ‘upper’ and ‘lower’ surfaces ( $y = \pm 0$ ) of the flag. Applying the Bernoulli equation and neglecting terms  $O(\partial^2 \xi/\partial x^2, \partial^2 \xi/\partial x \partial t)$  for consistency with the above approximation, we obtain for the non-circulatory pressure jump

$$\Delta p_{nc} = \frac{2x-1}{\sqrt{x(1-x)}} \left( \frac{1}{\alpha} \frac{\partial \xi}{\partial t} + \frac{\partial \xi}{\partial x} \right) - \frac{2}{\alpha^2} \sqrt{x(1-x)} \frac{\partial^2 \xi}{\partial t^2} \tag{4}$$

which preserves the square-root leading- and trailing-edge singularities together with the added-mass term. The significance of this approximation is discussed further in Section 5.

To obtain a finite velocity at the trailing edge, the circulatory flow associated with vortex shedding from the free end must be considered. The vortex is modelled as a vortex sheet and we let  $\gamma = \gamma(x_v, t)$  (with  $1 < x_v < \infty$ , see Fig. 1) denote the circulation per unit length of the wake. The circulatory velocity potential is then [12]

$$\phi_c = -\frac{1}{4\pi} \int_1^\infty \arctan \left( \frac{\sqrt{x(1-x)(x_v^2-1)}}{(1+x_v)/2 - xx_v} \right) \gamma(x_v, t) dx_v. \tag{5}$$

The circulation  $\gamma(x_v, t)$  is determined by the Kutta condition, requiring that no infinite velocities occur at the trailing edge. Therefore,

$$\left( \frac{\partial \phi_{nc}}{\partial x} + \frac{\partial \phi_c}{\partial x} \right)_{x=1} \text{ must be finite.}$$

Substitution of Eqs. (3) and (5) into the above yields the condition

$$\frac{1}{2\pi} \int_1^\infty \sqrt{\frac{x_v+1}{x_v-1}} \gamma(x_v, t) dx_v = \left( \frac{1}{\alpha} \frac{\partial \xi}{\partial t} + \frac{\partial \xi}{\partial x} \right)_{x=1}. \tag{6}$$

The circulatory pressure jump associated with  $\phi_c$  in Eq. (5) is

$$\Delta p_c = -\frac{1}{2\pi \sqrt{x(1-x)}} \int_1^\infty \frac{2x+x_v-1}{\sqrt{x_v^2-1}} \gamma(x_v, t) dx_v. \tag{7}$$

Making use of relation (6), we obtain

$$\Delta p_c = -\frac{2C(\gamma) - 1 + 2x(1 - C(\gamma))}{\sqrt{x(1-x)}} \left( \frac{1}{\alpha} \frac{\partial \xi}{\partial t} + \frac{\partial \xi}{\partial x} \right), \tag{8}$$

where  $C(\gamma)$  is the Theodorsen function [12]

$$C(\gamma) = \frac{\int_1^\infty \frac{x_v}{\sqrt{x_v^2 - 1}} \gamma(x_v, t) dx_v}{\int_1^\infty \sqrt{\frac{x_v + 1}{x_v - 1}} \gamma(x_v, t) dx_v}. \tag{9}$$

The total pressure jump is therefore given by

$$\Delta p = \Delta p_{nc} + \Delta p_c = -2C(\gamma) \sqrt{\frac{1-x}{x}} \left( \frac{1}{\alpha} \frac{\partial \xi}{\partial t} + \frac{\partial \xi}{\partial x} \right) - \frac{2}{\alpha^2} \sqrt{x(1-x)} \frac{\partial^2 \xi}{\partial t^2}. \tag{10}$$

### 2.2. End conditions

We examine solutions of Eq. (2) that satisfy either “fixed-free”

$$\xi(0, t) = 0, \quad \frac{\partial^2 \xi}{\partial x^2}(0, t) = 0, \quad \frac{\partial^2 \xi}{\partial x^2}(1, t) = 0, \quad \frac{\partial^3 \xi}{\partial x^3}(1, t) = 0 \tag{11}$$

or “clamped-free”

$$\xi(0, t) = 0, \quad \frac{\partial \xi}{\partial x}(0, t) = 0, \quad \frac{\partial^2 \xi}{\partial x^2}(1, t) = 0, \quad \frac{\partial^3 \xi}{\partial x^3}(1, t) = 0 \tag{12}$$

boundary conditions.

## 3. Temporal stability analysis

### 3.1. The eigenvalue problem

Assuming exponential time dependence

$$\xi(x, t) = \zeta(x) \exp[-i\omega t], \tag{13}$$

we obtain, respectively, from Eqs. (2) and (10)

$$-\omega^2 \zeta + \zeta'''' - \frac{\alpha^2}{\mu} \Delta \Pi = 0, \tag{14}$$

where a prime denotes differentiation with respect to  $x$  and

$$\Delta \Pi = -2C(\gamma) \sqrt{\frac{1-x}{x}} \left( -\frac{i\omega}{\alpha} \zeta + \zeta' \right) + \frac{2\omega^2}{\alpha^2} \sqrt{x(1-x)} \zeta. \tag{15}$$

The end-conditions are fixed-free:

$$\zeta(0) = \zeta''(0) = \zeta''(1) = \zeta'''(1) = 0, \tag{16}$$

or clamped-free:

$$\zeta(0) = \zeta'(0) = \zeta''(1) = \zeta'''(1) = 0. \tag{17}$$

3.1.1. No inertial fluid loading

Eq. (14) reduces to the familiar equation governing small oscillations of an elastic beam when  $\Delta\Pi = 0$ . This case is important because the associated eigenfunctions can be used to investigate the general fluid loaded and forced motions. When  $\Delta\Pi = 0$ , the general solution of Eq. (14) is [16]

$$\zeta_n(x) = a[\cos(k_n x) + \cosh(k_n x)] + b[\cos(k_n x) - \cosh(k_n x)] + c[\sin(k_n x) + \sinh(k_n x)] + d[\sin(k_n x) - \sinh(k_n x)], \tag{18}$$

where  $a, b, c, d$  and  $k_n$  are constants determined by the boundary conditions. For fixed-free conditions we find from Eq. (16) that  $a = b = 0$  and

$$\zeta_n(x) = \sin(k_n x) + \frac{\sin(k_n)}{\sinh(k_n)} \sinh(k_n x) \tag{19}$$

with  $k_n$  determined by the eigenvalue equation

$$\tan(k_n) - \tanh(k_n) = 0. \tag{20}$$

For clamped-free conditions, the application of Eq. (17) yields  $a = c = 0$  and

$$\zeta_n(x) = [\sin(k_n x) - \sinh(k_n x)] - \frac{\sin(k_n) + \sinh(k_n)}{\cos(k_n) + \cosh(k_n)} [\cos(k_n x) - \cosh(k_n x)] \tag{21}$$

with  $k_n$  satisfying

$$\cos(k_n) \cosh(k_n) + 1 = 0. \tag{22}$$

The amplitude of the motion described by either Eq. (19) or (21) is arbitrary.

It follows that the general unforced motion of the flag in the absence of unsteady fluid loading consists of a linear superposition of standing waves of the form

$$\xi_n = \zeta_n(x) \exp[-i\omega_n t], \quad \omega_n = k_n^2, \tag{23}$$

where  $\zeta_n, k_n$  are determined by either Eqs. (19)–(20) or (21)–(22).

3.1.2. Influence of inertial fluid loading

Consider a time harmonic solution of the type (13) and expand the amplitude  $\zeta(x)$  in terms of the eigenfunctions  $\zeta_n$

$$\zeta(x) = \sum_{n=1}^{\infty} a_n \zeta_n. \tag{24}$$

This automatically satisfies conditions (16) or (17). Substitute Eqs. (24) and (15) into Eq. (14) to obtain

$$\sum_{n=1}^{\infty} a_n (-\omega^2 + k_n^4) \zeta_n + 2 \frac{\alpha^2}{\mu} C(\gamma) \sqrt{\frac{1-x}{x}} \sum_{n=1}^{\infty} a_n \zeta_n' - 2 \frac{i\omega\alpha}{\mu} C(\gamma) \sqrt{\frac{1-x}{x}} \sum_{n=1}^{\infty} a_n \zeta_n - 2 \frac{\omega^2}{\mu} \sqrt{x(1-x)} \sum_{n=1}^{\infty} a_n \zeta_n = 0. \tag{25}$$

The coefficients  $a_n$  satisfy the infinite system of linear equations obtained by multiplying Eq. (25) by  $\zeta_m(x)$ , integrating over the flag ( $0 < x < 1$ ) and invoking the orthogonality relation (after writing  $\zeta_n$  in orthogonal form)

$$\int_0^1 \zeta_n \zeta_m dx = \delta_{mn}, \tag{26}$$

where  $\delta_{mn}$  is the Kronecker delta. This yields

$$a_m (-\omega^2 + k_m^4) + 2 \frac{\alpha^2}{\mu} C(\gamma) \sum_{n=1}^{\infty} a_n I_{mn} - 2 \frac{i\omega\alpha}{\mu} C(\gamma) \sum_{n=1}^{\infty} a_n \Phi_{mn} - 2 \frac{\omega^2}{\mu} \sum_{n=1}^{\infty} a_n \Psi_{mn} = 0 \tag{27}$$

for  $m = 1, 2, \dots$ , where

$$I_{mn} = \int_0^1 \zeta_m(x)\zeta'_n(x)\sqrt{\frac{1-x}{x}}dx, \tag{28}$$

$$\Phi_{mn} = \int_0^1 \zeta_m(x)\zeta_n(x)\sqrt{\frac{1-x}{x}}dx, \tag{29}$$

$$\Psi_{mn} = \int_0^1 \zeta_m(x)\zeta_n(x)\sqrt{x(1-x)}dx. \tag{30}$$

In accordance with Eq. (13) we assume exponential space and time dependence of the free vortex sheet, and write

$$\gamma(x_v, t) = \Gamma(\omega/\alpha) \exp\left[-i\omega t + i\frac{\omega}{2\alpha}x_v\right], \tag{31}$$

where  $\Gamma$  denotes the frequency-dependent vortex sheet strength. From Eq. (9) we then have

$$C(\omega/\alpha) = \frac{\int_1^\infty \frac{x_v}{\sqrt{x_v^2-1}} \exp[-i\omega x_v/2\alpha] dx_v}{\int_1^\infty \sqrt{\frac{x_v+1}{x_v-1}} \exp[-i\omega x_v/2\alpha] dx_v}. \tag{32}$$

The eigenfrequencies of self-excited motion are now calculated numerically by truncation of the eigenfunction expansion (24) and the homogeneous system (27) at a suitably large value of  $n = N$ , leading to a dispersion relation of the form  $\omega = \omega(k_1, \dots, k_N, \mu, \alpha)$  and formulae for the ratios of the coefficients  $a_1, \dots, a_N$ . Writing  $\omega = \omega_r + i\omega_i$ , in terms of its real and imaginary parts, we seek to describe the locus of the neutral surface,

$$\omega_i(k_1, \dots, k_N, \mu, \alpha, \omega_r) = 0, \tag{33}$$

across which instability sets in. For clarity of presentation, in much of the following  $\omega_r$  is replaced by the reduced frequency  $\Omega_r = \omega_r/\alpha$ , which is equivalent to normalizing the dimensional frequency by the inertial scale  $U/L$  rather than  $U_b/L$ . We also note that when substituting  $\omega_i = 0$ , Eq. (32) becomes [12]

$$C(\Omega_r) = \frac{H_1^{(2)}(\Omega_r/2)}{H_1^{(2)}(\Omega_r/2) + iH_0^{(2)}(\Omega_r/2)}, \tag{34}$$

and that  $\Gamma$  in Eq. (31), calculated by means of Eq. (6), is

$$\Gamma(\Omega_r) = 4 \frac{i\Omega_r\zeta(1) - \zeta'(1)}{H_1^{(1)}(\Omega_r/2) - iH_0^{(1)}(\Omega_r/2)}, \tag{35}$$

where  $H_j^{(i)}$  are Hankel functions of the  $j$ th kind and  $i$ th order.

### 3.2. Numerical results

Note that in calculating the neutral surface (33) the eigenvalues  $k_n$  for both fixed-free ( $\approx 3.93, 7.07, 10.21 \dots$ , see Eq. (20)) and clamped-free ( $\approx 1.86, 4.69, 7.85 \dots$ , see Eq. (22)) conditions are invariant, and therefore only the non-dimensional flag mass  $\mu$  and relative wind velocity  $\alpha$  can be prescribed. Our results indicate that excellent convergence of the numerical scheme is achieved when the series (24) is truncated at  $N \sim 20$  for all chosen combinations of  $(\mu, \alpha)$ .

In the following we examine both the quasi-steady aerodynamic approximation [17] and the full solution of the eigenvalue problem. The former considers the limit of a heavy flag ( $\mu \gg 1$ ) in a stiff wind ( $\alpha \gg 1$ ), such that  $\beta = \alpha/\sqrt{\mu}$  is finite. Physically, this approximation neglects all unsteady terms in expression (10) for the pressure jump, including the added mass contribution. This greatly simplifies the computations because

$C(\gamma) = 1$  (see Eq. (32)), and therefore Eq. (27) yields

$$a_m(-\omega^2 + k_m^4) + 2\beta^2 \sum_{n=1}^{\infty} a_n I_{nm} = 0. \tag{36}$$

The quasi-steady problem is accordingly governed by the single parameter  $\beta$  and can be formulated as a linear eigenvalue problem for  $\omega^2$ .

Fig. 2 illustrate the neutral surface (33) in (a) the  $(\mu, \alpha)$  plane and (b) the  $(\mu, \Omega_r)$  plane. The solid lines correspond to the full solution and the dashed curves denote the quasi-steady approximation. The thick and thin curves in each part of the figure correspond, respectively, to the application of the fixed-free and clamped-free boundary conditions. For each value of  $\mu$  there exists a critical value of the normalised wind speed  $\alpha = U/U_b = \alpha_c$  above which instability sets in. For all cases presented, the value of  $\alpha_c$  increases monotonically with  $\mu$ , leading to the intuitive result that heavier flags require a stronger wind to flap. The critical reduced frequency  $\Omega_{rc}$  at which instability is excited can be found from the corresponding point in Fig. 2b. In both the quasi-steady (dashed lines) and the full (solid lines) solutions this frequency decreases with  $\mu$ , indicating that heavier flags start flapping at lower frequencies.

A remarkable result evident from Fig. 2a is the significant stabilizing effect of the fixed boundary condition at the flag pole over the clamped case. Replacing the constraint of a vanishing angle of deflection at the pole with one of zero curvature introduces natural modes of higher frequency ( $\omega_n = \sqrt{k_n}$ ) and therefore more difficult to excite. Consequently, the value of  $\alpha_c$  in the fixed-free case exceeds by the factor of three the clamped-free value at a given  $\mu$  along most of the curve in the full solution and slightly less than that in the quasi-steady approximation. The differences in the critical reduced frequency are less substantial, although consistently higher values of  $\Omega_{rc}$  are observed for the clamped flag.

The quasisteady approximation yields lower critical  $\alpha_c$  values in both the fixed-free and the clamped-free cases. This is a consequence of the limit process that neglects the stabilizing effect of added-mass. Yet, this approximation supplies a qualitative picture of the full solution. Our numerical calculation yields for the critical quasi-steady contours in Fig. 2a the approximate formulae  $\alpha_c \approx 15.6\sqrt{\mu}$  ( $\beta_c \approx 15.6$ ) and  $\alpha_c \approx 5.99\sqrt{\mu}$  ( $\beta_c \approx 5.99$ ) corresponding, respectively, to the fixed-free and clamped-free cases. The latter differs considerably from the corresponding result obtained by Argentina and Mahadevan [11], who found  $\alpha_c \approx 10.53\sqrt{\mu}$  using a different numerical approach. The quasi-steady model is expected to agree quantitatively with the full solution when  $\mu, \alpha \gg 1$  and  $\Omega_r \ll 1$ . As can be seen from Fig. 2b, the latter condition is not satisfied at the presented range of  $\alpha$ , yielding the large discrepancies observed in Fig. 2a even for relatively large  $\mu$  and  $\alpha$ . It is only for considerably heavier flags that the quasi-steady approximation becomes a valid quantitative model.

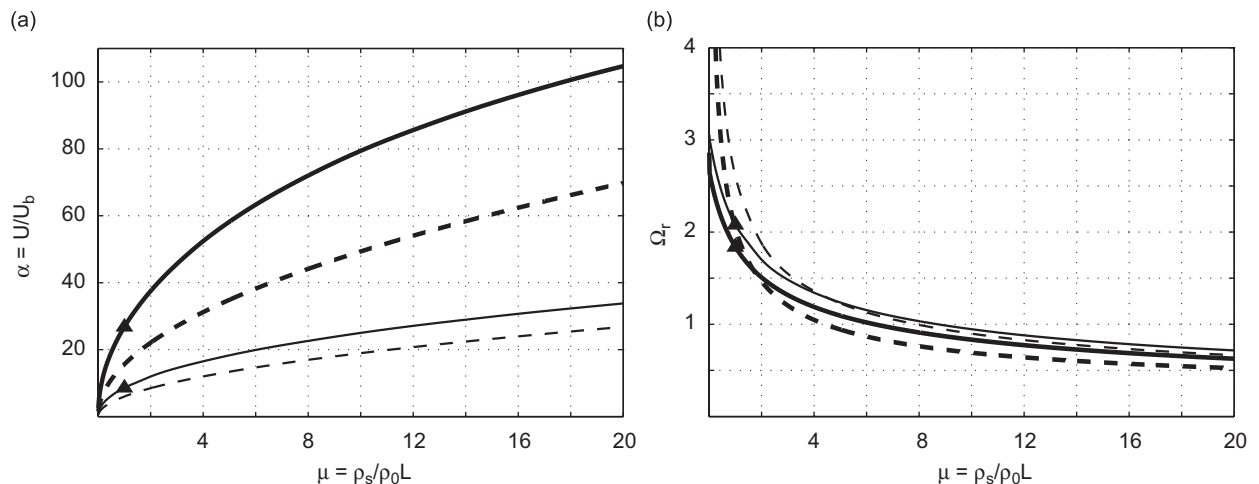


Fig. 2. The neutral surface in the (a)  $(\mu, \alpha)$  plane and the (b)  $(\mu, \Omega_r)$  plane for the quasi-steady (dashed) approximation and full (solid) problem. The bold and thin curves correspond, respectively, to the fixed-free and clamped-free conditions. The triangles indicate points later referred to in Fig. 4.

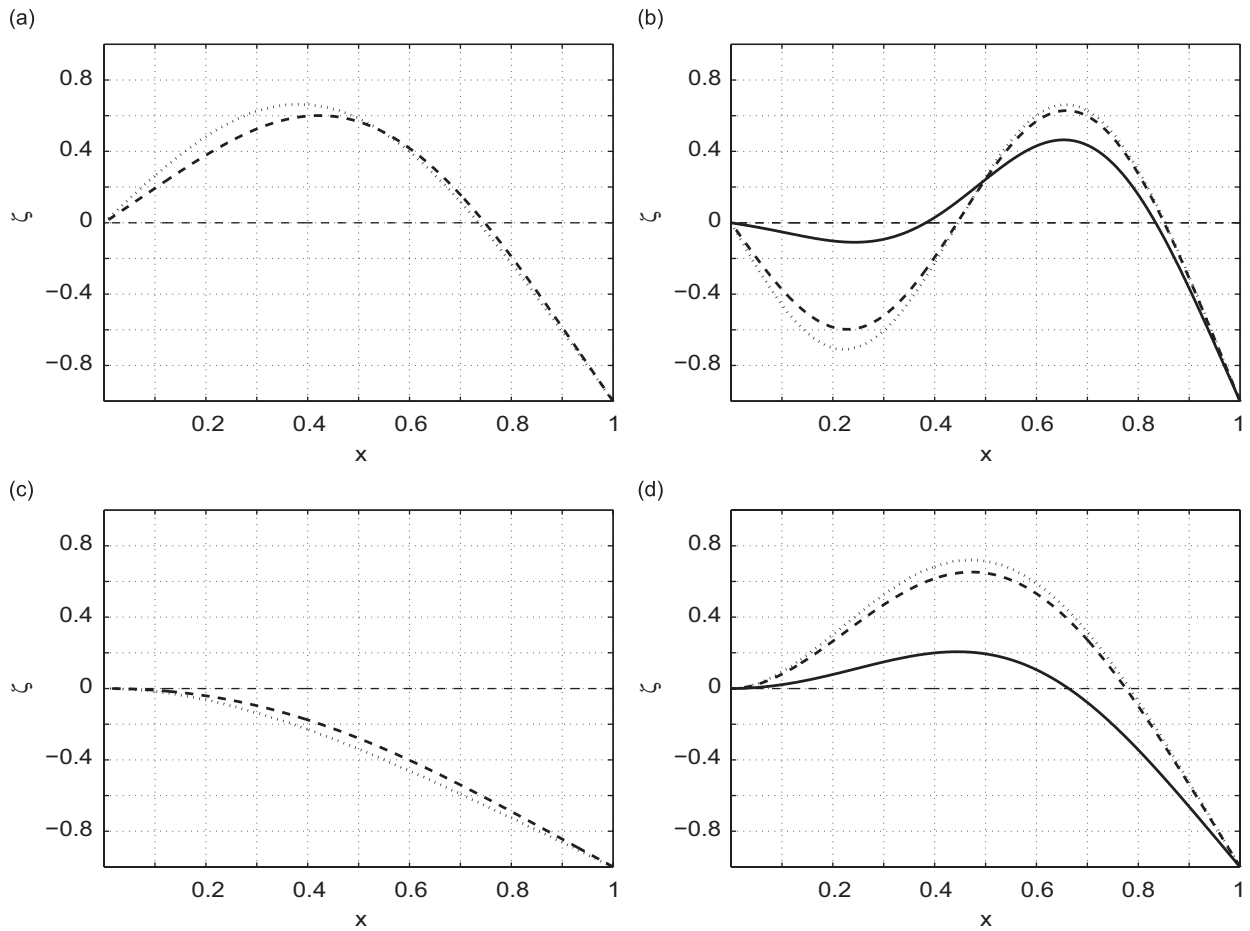


Fig. 3. The (a, c) first and (b, d) second modes of motion for the (a, b) fixed-free and (c, d) clamped-free conditions in the absence (dotted lines) and quasisteady approximation (dashed and solid curves) of inertial fluid loading. The dashed lines correspond to neutrally stable modes ( $\beta = 5, \omega = (18.6, 51.2)$  in (a,b);  $\beta = 2, \omega = (6.3, 22.5)$  in (c,d)) and the solid lines describe the unstable waves occurring at the onset of instability ( $\beta = 15.6, \omega = 54.9$  in (b);  $\beta = 5.99, \omega = 22.5$  in (d)). In the absence of fluid inertia, the frequencies corresponding to the low-order modes (dotted lines) are (15.4, 50.0) in (a,b) and (3.45, 22.0) in (c,d), respectively.

To gain further insight into the mechanism of transition to instability, we show in Fig. 3 the dependence of the low-order modes on the single parameter  $\beta$  in the quasi-steady approximation. Parts (a,b) of the figure correspond to the fixed-free problem and parts (c,d) are for the clamped-free case. The first and second modes of motion are given in parts (a, c) and (b, d), respectively. The dashed lines correspond to the stable sub-critical modes for some  $\beta < \beta_c$ , while the solid lines (in parts (b,d)) are the unstable modes for  $\beta = \beta_c$  (numerical values are given in the figure caption). The dotted curves in each figure correspond to the low-order modes in the absence of inertial fluid loading (see Eqs. (19) and (21)).

Our numerical calculations invariably yield real values for the eigenfrequencies in the sub-critical conditions of the quasi-steady solution. The corresponding modes are real functions for all  $\beta < \beta_c$  (dashed curves). At this sub-critical stage, we observe that the eigenfunctions are similar to their respective natural modes in the absence of inertial fluid loading (dotted lines). With increasing  $\beta < \beta_c$ , the lowest eigenvalues ( $\omega_r = 18.6, 6.3$  in the fixed-free and clamped-free cases, respectively) increase while their associated modes (dashed curves in parts (a, c)) change form. At the same time, the higher second eigenvalue varies only slightly. At the critical value  $\beta = \beta_c$  the first two eigenvalues collide on the real axis and split, leading to a resonance type of instability [18] manifested as a standing wave of increasing amplitude. For  $\beta > \beta_c$ , one of the modes becomes unstable, with a positive imaginary part and a non-vanishing real part. It is worthwhile to note the considerable

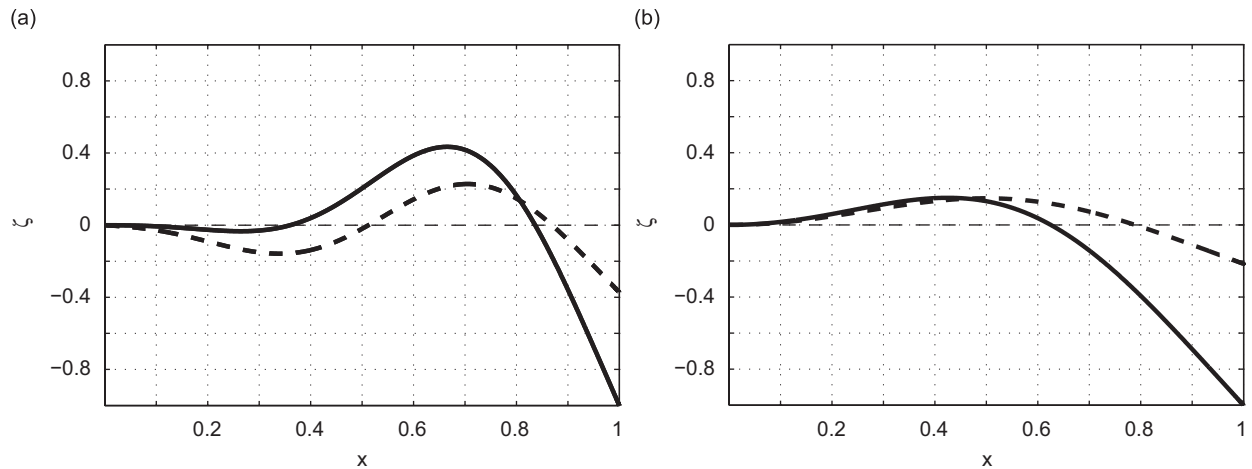


Fig. 4. The unstable modes of motion at the onset of instability in the complete problem for the (a) fixed-free ( $\mu = 1, \alpha = 26.8, \Omega_r = 1.84$ ) and (b) clamped-free ( $\mu = 1, \alpha = 8.60, \Omega_r = 2.08$ ) cases. Solid and dashed lines correspond to the real and imaginary parts of  $\zeta(x)$ , respectively.

differences between the modes in the fixed-free and clamped-free cases: although the qualitative mechanism of instability is similar in both cases, the impact of the different boundary conditions is clearly visible.

The description above may be valid for very heavy flags. The state of affairs changes considerably, however, when  $\mu \sim O(1)$ , for which it is necessary to solve the complete eigenvalue problem. To illustrate this, Fig. 4 presents the unstable modes of motion for the complete problem at the onset of instability for the fixed-free (Fig. 4a) and clamped-free (Fig. 4b) conditions. The critical behaviour is shown for the case  $\mu = 1$ , indicated by triangles in Fig. 2. Once again, the differences in the mode shapes for the different cases are evident. Unlike in the quasi-steady approximation, the sub-critical behaviour of the flag (i.e., when  $\alpha < \alpha_c$  for fixed  $\mu$ ) is stable: all eigenvalues lie in the lower half of the complex plane and the corresponding eigenfunctions contain *both* real and imaginary parts. At  $\alpha = \alpha_c$ , the lowest eigenmode becomes neutrally stable with  $\omega_i = 0$ . The solid and dashed lines in the figure correspond to the real and imaginary parts of this mode, respectively, which may also be interpreted as the respective shapes of the flag at  $t = 2\pi s/\omega_r$  and  $t = (\pi/2 + 2\pi s)/\omega_r$ , with  $s = 0, 1, 2, \dots$ . For  $\alpha > \alpha_c$ , flutter instability occurs, yielding *convecting* waves of increasing amplitude.

#### 4. The acoustic radiation

In this section we revert to dimensional coordinates for better clarity of presentation. Asterisks, attached to dimensional quantities in Section 2, are omitted for brevity.

The acoustic pressure is given in the linearised approximation at high Reynolds numbers by [19]

$$\begin{aligned}
 p_a(\mathbf{x}, t) &= p_{a_1}(\mathbf{x}, t) + p_{a_2}(\mathbf{x}, t) \\
 &= \rho_0 \frac{\partial}{\partial t} \int_{-\infty}^{\infty} \oint_S v_n(\mathbf{y}, \tau) G_a(\mathbf{x}, \mathbf{y}, t - \tau) dS(\mathbf{y}) d\tau - \rho_0 \int_{-\infty}^{\infty} \int_V (\boldsymbol{\omega} \times \mathbf{U}) \cdot \nabla G_a(\mathbf{x}, \mathbf{y}, t - \tau) d^3\mathbf{y} d\tau, \quad (37)
 \end{aligned}$$

where  $S$  is the surface of the flag,  $v_n(\mathbf{y}, \tau)$  its normal velocity directed into the fluid and  $G_a(\mathbf{x}, \mathbf{y}, t - \tau)$  the acoustic Green's function having vanishing normal derivative on the undisturbed flag. The first integral,  $p_{a_1}(\mathbf{x}, t)$ , is the pressure contribution due to the flag motion;  $p_{a_2}(\mathbf{x}, t)$ , given by the second integral, is the pressure produced by the wake.  $V$  denotes the fluid region occupied the wake,  $\boldsymbol{\omega}$  is the vorticity and  $\mathbf{U}$  is the mean stream velocity.

When the frequency of the oscillations is small enough that the flag is acoustically compact, the compact approximation [19]

$$G_a(\mathbf{x}, \mathbf{y}, t - \tau) = \frac{1}{4\pi|\mathbf{X} - \mathbf{Y}|} \delta\left(t - \tau - \frac{|\mathbf{X} - \mathbf{Y}|}{c_0}\right) \quad (38)$$

may be applied to evaluate the far-field acoustic radiation. Here  $\mathbf{X}(\mathbf{x})$  and  $\mathbf{Y}(\mathbf{y})$  denote the Kirchhoff vectors for the flag and  $c_0$  is the speed of sound. Substitute Eq. (38) into the integral for  $p_{a1}(\mathbf{x}, t)$  and expand to first order in  $\mathbf{Y}$  as  $|\mathbf{X}| \sim |\mathbf{x}| \rightarrow \infty$ , to obtain

$$p_{a1}(\mathbf{x}, t) \approx \frac{\rho_0}{4\pi|\mathbf{x}|} \frac{\partial}{\partial t} \oint_S v_n \left( \mathbf{y}, t - \frac{|\mathbf{x}|}{c_0} \right) dS(\mathbf{y}) + \frac{\rho_0 x_j}{4\pi c_0 |\mathbf{x}|^2} \cdot \frac{\partial^2}{\partial t^2} \oint_S v_n \left( \mathbf{y}, t - \frac{|\mathbf{x}|}{c_0} \right) Y_j(\mathbf{y}) dS(\mathbf{y}). \tag{39}$$

The first integral, representing a monopole, vanishes because the volume of the flag is constant. The acoustic far-field is therefore of dipole type, determined by the second integral. We approximate  $\mathbf{Y}(\mathbf{y})$  by the Kirchhoff vector for a strip of unit width

$$\mathbf{Y}(y_1, y_2) = \left( y_1, \text{Re} \left[ -i \sqrt{\left( y_1 - \frac{L}{2} + iy_2 \right)^2 - \frac{L}{4}}, y_3 \right] \right), \tag{40}$$

where  $y_1, y_2, y_3$  are the components of the  $\mathbf{y}$ -vector in the streamwise  $\hat{\mathbf{y}}_1$ , flapping  $\hat{\mathbf{y}}_2$  and spanwise  $\hat{\mathbf{y}}_3$  directions, respectively. Along the flag  $y_2 = \pm 0$ ,  $dS = dy_1 dy_3$ ,  $0 \leq y_1 \leq L$  and  $0 \leq y_3 \leq l$ . In addition,

$$v_n(y_1, t; \omega) = \mp i \omega \exp[-i\omega t] \sum_{n=1}^{\infty} a_n \zeta_n(y_1) \quad \text{at } y_2 = \pm 0$$

(see (24)). Writing  $x_2 = |\mathbf{x}| \cos \theta$  (with  $0 \leq \theta \leq \pi$  indicating the observer direction), we find

$$\frac{p_{a1}(|\mathbf{x}|, \theta, t; \omega)}{\rho_0 U^2} \approx M \frac{l \cos \theta}{2\pi|\mathbf{x}|} \exp \left[ -i\omega \left( t - \frac{|\mathbf{x}|}{c_0} \right) \right] F_1(\omega), \quad |\mathbf{x}| \rightarrow \infty, \tag{41}$$

where  $M = U/c_0 \ll 1$  is the mean stream Mach number and

$$F_1(\omega) = i \left( \frac{\omega}{U} \right)^3 \sum_{n=1}^{\infty} a_n \int_0^L \zeta_n(y_1) \sqrt{y_1(L-y_1)} dy_1 = i \left( \frac{\omega L}{U} \right)^3 \sum_{n=1}^{\infty} a_n \int_0^1 \frac{\zeta_n(\bar{y}_1)}{L} \sqrt{\bar{y}_1(1-\bar{y}_1)} d\bar{y}_1. \tag{42}$$

To calculate  $p_{a2}(\mathbf{x}, t)$ , write

$$\boldsymbol{\omega} = \gamma(y_1, t) \delta(y_2) \hat{\mathbf{y}}_3, \quad \mathbf{U} = U \hat{\mathbf{y}}_1, \quad 0 \leq y_3 \leq l \tag{43}$$

to obtain

$$p_{a2}(\mathbf{x}, t) = -\rho_0 U \int_{-\infty}^{\infty} \oint_S \gamma(y_1, \tau) \frac{\partial G_a}{\partial y_2}(\mathbf{x}, \mathbf{y}, t - \tau) dS d\tau, \tag{44}$$

where  $S$  denotes the surface of the wake ( $y_2 = \pm 0$ ,  $1 \leq y_1 < \infty$  and  $0 \leq y_3 \leq l$ ).

Substituting (38) in conjunction with (31) and (40) into (44) and following a procedure similar to the one outlined above for  $p_{a1}(\mathbf{x}, t)$ , yields

$$\frac{p_{a2}(|\mathbf{x}|, \theta, t; \omega)}{\rho_0 U^2} \approx M \frac{l \cos \theta}{2\pi|\mathbf{x}|} \exp \left[ -i\omega \left( t - \frac{|\mathbf{x}|}{c_0} \right) \right] F_2(\omega), \tag{45}$$

where

$$\begin{aligned}
 F_2(\omega) &= i \frac{\omega \Gamma(\omega)}{U^2} \int_L^\infty \left( \frac{\partial Y_2}{\partial y_2} \right)_{y_2=0} \exp[i\omega y_1/2U] dy_1 \\
 &= i \frac{\omega L \Gamma(\omega)}{U} \int_1^\infty \frac{\bar{y}_1 - 1/2}{\sqrt{\bar{y}_1(\bar{y}_1 - 1)}} \exp[i\omega L \bar{y}_1/2U] d\bar{y}_1 \\
 &= -\frac{i\pi \omega L \Gamma(\omega)}{4 U} \exp[i\omega L/4U] H_1^{(1)}(\omega L/4U).
 \end{aligned}
 \tag{46}$$

The total far-field pressure for a compact flag is therefore approximated to first order by the dipole field

$$p_a(|\mathbf{x}|, \theta, t; \omega) \approx M \frac{l \cos \theta}{2\pi |\mathbf{x}|} \exp \left[ -i\omega \left( t - \frac{|\mathbf{x}|}{c_0} \right) \right] F(\omega), \quad |\mathbf{x}| \rightarrow \infty,
 \tag{47}$$

where  $F = F_1 + F_2$  is given by the sum of Eqs. (42) and (46).

The frequency dependence of  $F_1$ ,  $F_2$  and  $F$  at the onset of instability (where  $\omega L/U = \Omega_r$ ) are illustrated in Fig. 5 for the two cases of (a, c) fixed-free and (b, d) clamped-free conditions. The solid and dashed curves correspond to the real and imaginary parts of the functions and the dash-dotted lines show the quasisteady (real) solution

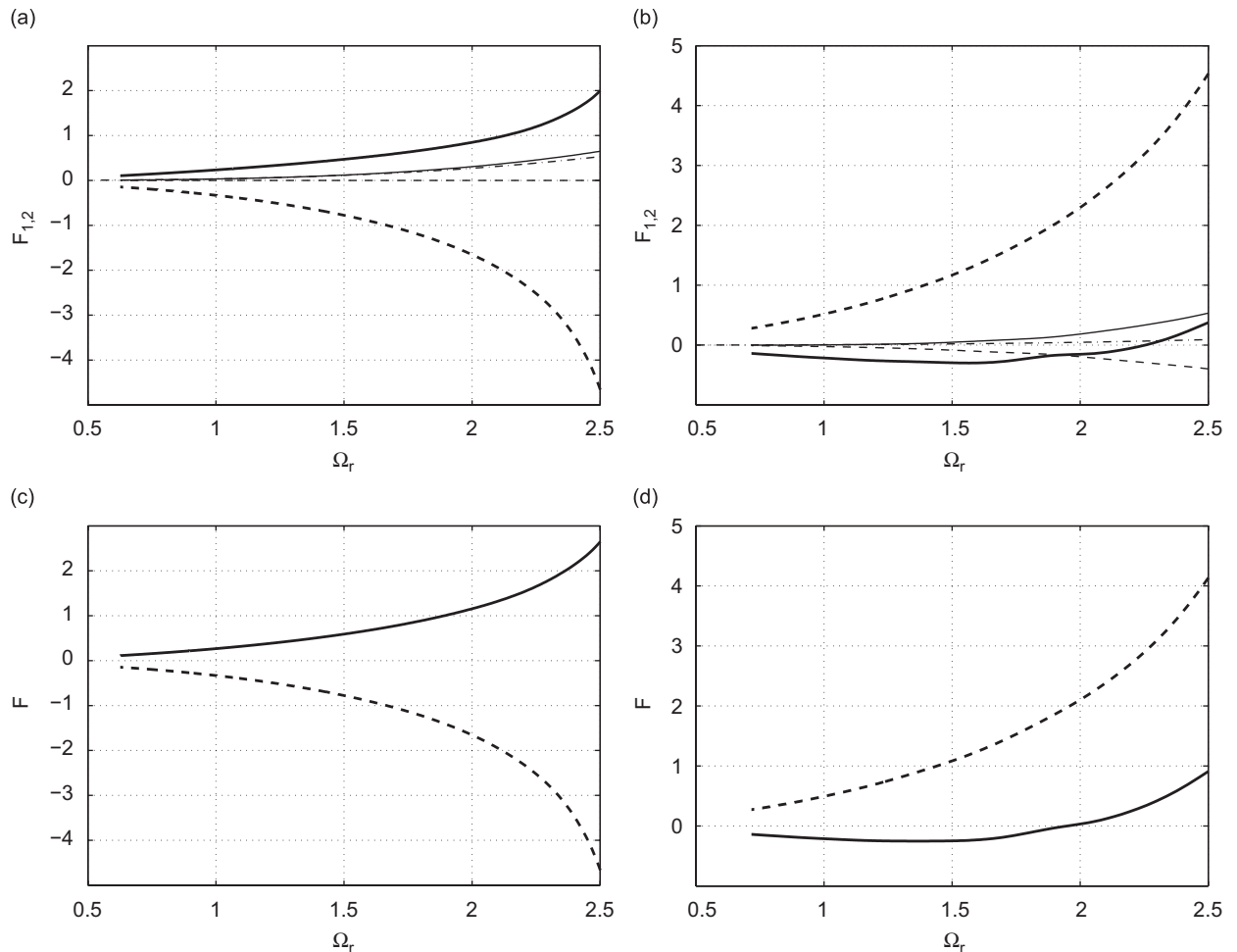


Fig. 5. The functions (a,b)  $F_1$  (thick lines),  $F_2$  (thin curves) and (c, d)  $F$  at the onset of instability in the (a, c) fixed-free and (b,d) clamped-free cases. The solid and dashed curves correspond to the real and imaginary parts of the functions and the dash-dotted lines describe the quasisteady (real) solution.

solution. The amplitude of the acoustic pressure increases with the critical reduced frequency  $\Omega_{r_c}$ . Recalling that  $\Omega_{r_c}$  itself increases when the flag is lighter (see Fig. 2b), it follows that heavier flags are less noisy than light flags at the onset of motion. There are no significant differences in the overall acoustic amplitudes between the fixed-free and clamped-free cases. However, the wake term,  $F_2$ , is significantly larger than the irrotational flag motion term,  $F_1$ , for all values of  $\Omega_r$  (Fig. 5a,b). Hence, the inclusion of the circulatory pressure jump (8) and the application of the Kutta condition (6) in our model is vital for the calculation of the far-field radiation. The quasi-steady approximation is close to the complete solution only for small frequencies, where the acoustic radiation becomes negligible and  $\alpha \gg 1$ . These conditions are indeed in agreement with the above-mentioned limitations of this approximation (see Section 3.2), expected to be valid only for very heavy flags.

## 5. Concluding remarks

We have presented a linear theory for the two-dimensional motion and sound production of an unforced elastic flag in nominally uniform high Reynolds number flow. The analysis permits the calculation of motion and sound production at the very onset of instability, but it cannot determine the resulting final states. Such predictions require consideration of a full nonlinear model, of the type suggested in Refs. [13,14]. In addition, three-dimensional “edge effects” of the flag motion have not been considered. These are important when the flag aspect ratio  $l/L$  becomes finite. Argentina and Mahadevan [11] have used an approximate calculation to demonstrate that decreasing  $l/L$  results in fluid loading rescaling which, in turn, stabilises the reference state. Although their calculation was limited to a clamped-free flag, it seems reasonable that a similar trend will be followed in the fixed-free case. A similar study of three-dimensional effects on the acoustic field may require a detailed calculation of the vorticity distributions along the edges of the flag in the spanwise direction.

In addition to the neglect of nonlinear and three-dimensional effects, the main drawback of our theory is the use made of Eq. (3) to describe the inertial pressure jump across the flag. Essentially, this approximation neglects the curvature ( $O(\partial^2 \xi / \partial x^2)$ ) and time rate of change of the local flag deflection angle ( $O(\partial^2 \xi / \partial x \partial t)$ ), as well as higher-order terms. A more general treatment would involve the use of a non-local representation of the potential, requiring integration over the whole flag.

Our use of hypothesis (3) follows the simplified model proposed by Theodorsen [12] and applied recently by Argentina and Mahadevan [11] to study the onset of motion and sound production for different choices of boundary conditions. The results obtained indicate that a flag that is merely fixed at its pole is considerably more stable than one that is clamped. In the quasi-steady limit of a very heavy flag, instability sets in as a resonance (standing wave of increasing amplitude), while lighter flags exhibit flutter (convective) instability. At the onset of flag motion the dipole-type acoustic far-field of a compact flag is dominated by wake sources. The application of the Kutta condition is therefore of crucial importance in determining the sound. Light flags, characterised by high critical frequencies, are predicted to produce more sound than heavy flags.

In practice the flag motion is likely to be significantly different from the simple homogeneous model studied here and in most previous investigations because of the neglect of “forcing” by discrete vortex structures shed quasi-periodically from the flag pole and convected in the mean stream over the surfaces of the flag. For a pole of diameter  $D$  in a mean stream  $U$ , the characteristic frequency of vortex shedding satisfies  $\omega^* D / U \approx 0.4\pi \approx 1.25$ . The resulting flag oscillations at this frequency accordingly correspond to  $\Omega_r \equiv \omega^* L / U \approx 1.25L / D \gg 1$ , very much larger than the typical homogeneous flag stability frequencies of Fig. 2. This suggests that the much more rapid effects of external forcing on the flag by flag-pole vortex shedding are likely to destroy the delicate equilibrium between bending stiffness and inertia needed for the validity of the homogeneous stability theory. It may be, therefore, that weak effects of flag stiffness (and also of drag-induced tension) become negligible and that the actual motion of a flag in a stiff breeze is due to a balance between the influence of shed vorticity from the flag pole and the combined effects of flag and fluid-loading inertia.

## References

- [1] M.P. Paidoussis, *Fluid–Structure Interaction: Slender and Axial Flow*, Academic Press, New York, 1998.
- [2] L. Huang, Flutter of cantilevered plates in axial flow, *Journal of Fluids and Structures* 9 (1995) 127–147.

- [3] Y. Watanabe, S. Suzuki, M. Sugihara, Y. Sueoka, An experimental study of paper flutter, *Journal of Fluids and Structures* 16 (2002) 529–542.
- [4] J.C. Liao, D.N. Beal, G.V. Lauder, M.S. Triantafyllou, Fish exploiting vortices decrease muscle activity, *Science* 302 (2003) 1566–1569.
- [5] L. Shen, X. Zhang, D.K.P. Yue, M.S. Triantafyllou, Turbulent flow over a flexible wall undergoing a streamwise traveling wave motion, *Journal of Fluid Mechanics* 484 (2003) 197–221.
- [6] S. Taneda, Waving motions of flags, *Journal of the Physical Society of Japan* 24 (1968) 392–401.
- [7] J. Zhang, S. Childress, A. Libchaber, M. Shelley, Flexible filaments in a flowing soap film as a model for one-dimensional flags in a two-dimensional wind, *Nature* 408 (2000) 835–839.
- [8] L. Zhu, C.S. Peskin, Simulation of a flapping flexible filament in a flowing soap film by the immersed boundary method, *Journal of Computational Physics* 179 (2002) 452–468.
- [9] Y. Watanabe, K. Isogai, S. Suzuki, M. Sugihara, A theoretical study of paper flutter, *Journal of Fluids and Structures* 16 (2002) 543–560.
- [10] M. Shelley, N. Vandenberghe, J. Zhang, Heavy flags undergo spontaneous oscillations in flowing water, *Physical Review Letters* 94 (2005) 094302.
- [11] M. Argentina, L. Mahadevan, Fluid-flow-induced flutter of a flag, *Proceedings of the National Academy of Science* 102 (2005) 1829–1834.
- [12] T. Theodorsen, 1935 General theory of aerodynamic instability and the mechanism of flutter. NACA Report no. 496.
- [13] B.H. Connell, D.K.P. Yue, Flapping dynamics of a flag in a uniform stream, *Journal of Fluid Mechanics* 581 (2007) 33–67.
- [14] S. Alben, M. Shelley, Flapping states of a flag in an inviscid fluid: bistability and the transition to chaos, *Physical Review Letters* 100 (2008) 074301.
- [15] A.D. Fitt, M.P. Pope, The unsteady motion of two-dimensional flags with bending stiffness, *Journal of Engineering and Mathematics* 40 (2001) 227–248.
- [16] J.W.S. Rayleigh, *The Theory of Sound*, Dover, New York, 1945.
- [17] R.L. Bisplinghoff, H. Ashley, R.L. Halfman, *Aeroelasticity*, Addison-Wesley, Reading, MA, 1955.
- [18] J.E. Marsden, T.S. Ratiu, *Introduction to Mechanics and Symmetry*, Springer, Berlin, 1994.
- [19] M.S. Howe, *Theory of Vortex Sound*, Cambridge University Press, Cambridge, 2003.